ADVANCED MATERIALS INTERFACES
www.advmatinterfaces.de

Probing Surfactant Bilayer Interactions by Tracking Optically Trapped Single Nanoparticles

*Jeonghyeon Kim and Olivier J. F. Martin**

Single-particle tracking and optical tweezers are powerful techniques for studying diverse processes at the microscopic scale. The stochastic behavior of a microscopic particle contains information about its interaction with surrounding molecules, and an optical tweezer can further facilitate this observation with its ability to constrain the particle to an area of interest. Although these techniques found their initial applications in biology, they can also shed new light on microscopic interface phenomena by unveiling nanoscale morphologies and molecular-level interactions in real time, which are obscured in traditional ensemble analysis. Here, the application of single-particle tracking and optical tweezers are demonstrated for studying molecular interactions at solid–liquid interfaces. Specifically, the surfactant behaviors at the water–glass interface are investigated by tracing gold nanoparticles that are optically trapped on these molecules. The underlying mechanisms governing the particle motion, which can be explained by hydrophobic interactions, disruptions, and rearrangements among surfactant monomers at the interfaces, are discovered. These interpretations are further supported by statistical analysis of an individual trajectory and comparison with theoretical predictions. The findings provide new insights into the surfactant dynamics and also illustrate the promise of single-particle tracking and optical manipulation for studying nanoscale physics and chemistry of surfaces and interfaces.

1. Introduction

The motion of a microscopic particle suspended in a medium provides information about its interactions with its surroundings.[1,2] It can be a purely random movement like the Brownian motion, but it can also be as complicated as hopping lipids on a cell membrane.[3] Measuring trajectories of single particles such as polystyrene beads,[4,5] gold nanoparticles,[6,7] fluorescent proteins,[8,9] and quantum dots[10] has revealed fundamental processes and microscopic structures in nature.[11–14] Thus, the observation of individual trajectories, known as single-particle tracking (SPT), has established itself as a powerful tool to study molecular processes and interactions, especially in biological systems.[2,8,11,12,15] Moreover, SPT holds great promise for studying nanoscale chemical and physical processes,[5,16–18] and novel applications of SPT are still actively emerging.[15]

An optical tweezer is another useful tool in single-molecule studies, which provides a non-invasive way of manipulating microscopic objects with great precision.[19–24] It combines a Gaussian laser beam with a high numerical aperture objective lens to produce a tight focal spot, which creates an optical force that can bring small objects to the intensity maximum.[25] Beyond the original capabilities to grab tiny objects,[26,27] optical tweezers have found diverse applications enabled by its ability to locally apply precise and controlled forces, ranging from measuring piconewton forces in molecular motors[28] to stretching or relaxing DNA to determine its elastic properties.[29]

Therefore, the utilization of optical tweezers in SPT experiments brings important advantages in giving a tracer particle pinpoint access to an area of interest and providing controlled forces to facilitate observation. After their initial and major applications in biophysics,[24,30,31] optical tweezers and SPT are being increasingly implemented together in physics such as microrheology[32] and hydrodynamics.[33] Franosch et al.,[5] for instance, studied the Brownian motion of an optically trapped bead in water and revealed that surrounding water molecules act back on the particle once disturbed by the particle's thermal motion. In particular, the optical tweezer played a crucial role in their discovery of such weak interactions by providing controlled forces and thus facilitating the characterization of the particle motion.

Unlike these successful demonstrations in biophysics and physics, the combination of optical tweezers and SPT has not yet actively emerged in chemistry and surface science. The SPT alone has been extensively used in surface science to unveil molecular-level details of diffusion,[34,35] mass transport,[18] catalytic reactions,[36] and many other processes,[37] which were inaccessible with classical bulk or ensemble measurements.[38] On the other hand, optical trapping has also found

J. Kim, O. J. F. Martin
Nanophotonics and Metrology Laboratory
Swiss Federal Institute of Technology Lausanne (EPFL)
Lausanne 1015, Switzerland
E-mail: olivier.martin@epfl.ch

The ORCID identification number(s) for the author(s) of this article can be found under https://doi.org/10.1002/admi.202201793.

DOI: 10.1002/admi.202201793

its distinctive applications, such as in Raman spectroscopy[39,40] and photo-catalysis.[41] Despite these various attempts, a marriage of optical tweezers and SPT has yet to be implemented, but their marriage holds great promise for monitoring the time evolution of chemical reactions at the microscopic scale.

Here, we demonstrate the combined application of optical tweezers and SPT to probe surface interactions at an interface. We study a specific case of optically trapped gold nanoparticles, which also serve as an optical probe for SPT, interacting with surfactant molecules adsorbed at a water–glass interface. Surfactants exist both on the glass walls of liquid containers and on the surfaces of the particles, spontaneously forming assembled structures.[42–45] We bring these heterogeneous surfaces close to each other by positioning a single particle at a time near a glass wall using an optical tweezer. We monitor the particle trajectories and investigate any anomalous behaviors in particle motions due to the local interaction of the surfactant molecules. We first demonstrate the effect of adsorption states on particle motion by showing a qualitative correlation between the thermodynamic model of adsorption and the statistics of measured single-particle trajectories. Furthermore, individual trajectories show evidence of long-term interactions between adsorbed molecules enforced by stable and long trapping of the particles near the interface. This long-term interaction exclusively occurs between incomplete surfactant bilayers on particle and glass surfaces, suggesting a possibility of the fusion of the bilayers on different surfaces. Finally, we perform statistical analyses on the time-averaged mean squared displacement of a single-particle trajectory, strengthening our interpretation of long-term bilayer interactions.

2. Results and Discussion

2.1. Surfactant Adsorption at Water–Glass Interface

Surfactant molecules adsorb at water–glass interfaces, spontaneously forming complex structures.[46] One of our hypotheses is that the morphology of surfactant self-assemblies can influence the particle–surface interactions. We examine this effect by altering the structure of the adsorbed molecules and comparing the subsequent particle movements. Cetyltrimethylammonium chloride (CTAC) was used as an example of cationic surfactants.

The self-assembly structures of the adsorbed molecules depend on several factors such as pH,[47] salt,[48,49] and surface preparation.[50,51] The change of solution pH or salinity can alter the overall surfactant self-assemblies on both the particles' surfaces and the glass walls. In contrast, the surface treatments on glass surfaces can provide a selective modification of adsorbed surfactants on the treated glass walls. Therefore, we used the latter approach to examine any changes in the particle–surface interactions due to a structural change of self-assemblies on glass surfaces while keeping the surface characteristics of the particles the same.

We prepared two different glass surfaces, and surfactants form either spherical aggregates or bilayer membranes depending on the properties of the glass surfaces (**Figure 1**). The first type of glass surface is a native glass without any surface modification. In general, a glass surface becomes negatively charged when immersed in water through the deprotonation of its silanol groups:[52]

$$\mathrm{SiOH} \rightleftharpoons \mathrm{SiO^-} + \mathrm{H^+} \tag{1}$$

In case of cationic surfactants, the negatively charged silanol (SiO^-) groups drive the initial adsorption through the electrostatic attraction with the cationic surfactant head groups. The adsorption of cationic molecules reduces the overall surface charge, and once the surface becomes neutralized, these molecules act as nucleation points for further adsorption.[46] At this stage, the hydrophobic interactions among surfactant tail groups drive the adsorption, similar to micelle formation in bulk solution. The molecules start to form centrosymmetric aggregates,[43] aka admicelles, as shown in Figure 1a. The surface coverage rises steeply by forming these admicelles in this concentration span, and it soon reaches saturation near the critical micellar concentration (CMC).

The second type of glass surface is modified by oxygen-plasma treatment to increase the number of silanol groups on its surface.[53] Henceforth, we call this type of glass an activated glass. After the plasma treatment, the activated surface becomes superhydrophilic due to the increased charged groups. We empirically tested the contact angle with water after

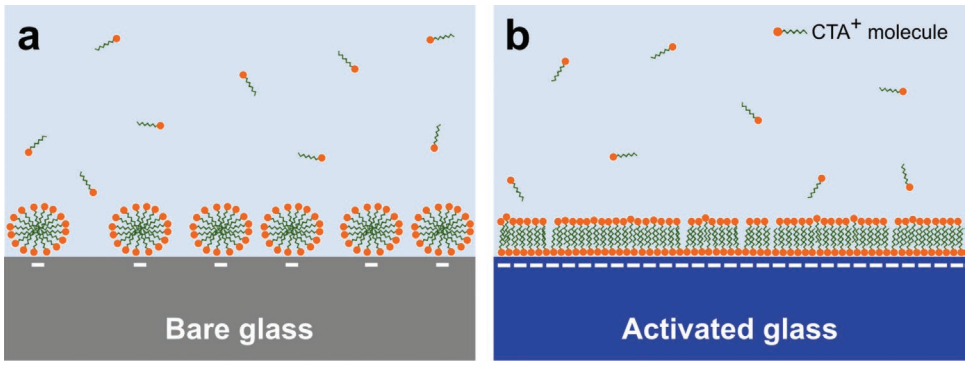

Figure 1. Schematic diagram showing probable morphologies of adsorbed surfactant molecules at the glass–water interface. a) A bare glass and b) a glass surface treated with oxygen (O_2) plasma. The activated glass surface has denser silanol groups compared to the native glass. These silanol (SiO^-) groups on each surface act as electrostatic binding sites for cationic surfactant adsorption.

oxygen-plasma treatment and observed complete wetting with a 0° contact angle (Figure S1, Supporting Information).

When such an activated glass is immersed in surfactant solution, the electrostatic attraction drives the initial adsorption like the adsorption with native glasses. We postulate that the adsorbed molecules are so close together that they form a quasi-continuous film. In experiments, we observed an immediate increase in the contact angle with surfactant solution compared to the 0° contact angle with water. Figure S1, Supporting Information shows the contact angle with the activated glass as a function of CTAC concentration, which increases with the concentration until it reaches saturation at 1 mM. Such an increase implies that a surfactant monolayer is formed with hydrophilic head groups electrostatically adsorbed to the surface and hydrophobic tail groups facing toward the bulk liquid. Any further adsorption that is hydrophobically driven forms a second layer above the first one (Figure 1b), rather than clustering as discrete aggregates as was the case for the bare glass (Figure 1a).

Such changes in self-assembly morphologies induced by the surface properties have been extensively studied in the literature.[42,49,51] Ducker et al.[42] studied surfactant (cetrimonium bromide, CTAB) aggregates on mica using AFM imaging. They found a transition from a flat bilayer to cylinders when reducing the binding sites on mica by introducing electrolyte (KBr). Lamont et al.[49] reported similar findings where they observed sequential changes in the structures of CTAC on mica (bilayer → ordered cylinder → disordered cylinder → short cylinder → sphere) on the addition of rival cations (Cs^+). Lastly, Grant et al.[51] investigated the influence of surface hydrophobicity on the aggregate structures of nonionic surfactants where hydrophobic interactions are the main adsorption driving force. They observed the evolution of adsorbed structures from diffuse spherical aggregates to a monolayer with increasing surface hydrophobicity. All these findings deliver the same message that the increase in active binding sites on surfaces leads to lower-curvature structures. Based on these ideas, we postulate that CTAC forms a bilayer structure on activated glass and discrete globular aggregates on bare glass as illustrated in Figure 1.

2.2. Particle Trajectory in a Harmonic Optical Trap

We used gold nanoparticles (150 nm average diameter) as an optical probe in this study. They scatter visible light resonantly, making their scattering cross sections much larger than their physical cross-sections and thus having been successfully utilized as nanoscale probes under optical microscopes.[6,7,13,54] They are also free from photobleaching or photoblinking, which enables long and continuous measurements, unlike their fluorescence counterparts.[55]

An optical tweezer was employed to confine the motion of a particle in a local domain and facilitate monitoring the particle's trajectory. Without an optical tweezer, the gold nanoparticles did not stay in the interfacial area due to electrostatic repulsion and also because of fast Brownian motions at such a small size. We emphasize that the optical tweezer not only provided a lateral confinement (parallel to the glass–water interface) but also a vertical confinement (normal to the interface) by constantly pushing the particle towards the glass surface with its radiation pressure. These lateral and vertical confinements significantly increased the chances of particle–surface interaction and enabled monitoring *long-term* phenomena. The optical trapping and imaging system is described in detail in the Experimental Section (Section 4).

Figure 2a shows an example time-series position data extracted from a single-particle video recording. (An example image and feature-finding process are illustrated in Figure S2, Supporting Information. More example trajectories are shown in Figure S3, Supporting Information.) Each position data point is color-mapped, gradually changing from yellow to dark blue for legibility. The position fluctuation inside the optical trap decreases over a timespan of 40 s in Figure 2a. Such changes with time deviate from a simple diffusion model and can be related to the interaction that the particle undergoes with its surroundings, especially with the molecules adsorbed on the glass wall. In other words, without surface interactions, the distribution would remain the same, only restricted by the optical trap, with no temporal dependence.

To quantitatively assess the time-dependent position data, we defined a radial displacement, r_t, as the distance from the origin (corresponding to the trap center) to the particle position ($X(t)$, $Y(t)$) where the XY-plane is a plane parallel to the glass–water interface:

$$r_t = \sqrt{X(t)^2 + Y(t)^2} \tag{2}$$

Figure 2b shows the evolution of r_t for the same trajectory in Figure 2a. The gradual decrease in the envelope of r_t depicts well the temporal changes in the particle motion inside the optical trap. Since r_t fluctuates between its extremes, we calculated the moving average of r_t to smooth out the short-term fluctuations and quantify its long-term decrease. We used a time window of 5 s (corresponding to 1730 data points) to calculate the moving average, $\overline{r_t}$, and plotted it as the red-dashed line in Figure 2b.

Interestingly, such changes in particle motions occur only with activated glass surfaces. For a bare glass substrate at the same CTAC concentration—shown in the inset of Figure 2b—there is no apparent change in the average radial displacement, $\overline{r_t}$ (the solid grey line in the inset). This difference between the native and activated glasses indicates that the structure of the adsorbed surfactants at the water–glass interface plays a role in the particle–surface interactions.

In addition, the absence of any changes in $\overline{r_t}$ for the bare glass case indicates that some long-term effects of the optical tweezer, such as optical heating, are still negligible in our experimental conditions. (To be more precise, the optical heating itself is not negligible based on our previous study comparing thermal and non-thermal probes,[56] and in fact, it can accelerate the interactions by providing thermal energy. However, the thermal equilibrium is reached almost instantaneously compared to the timescale discussed in the present study, which we confirmed by optical heating simulations (Section S5, Supporting Information). Therefore, we can say that the optical heating has no long-term effect.)

The hypothesis that the particle–surface interaction is sensitive to the surfactant morphologies can be tested in two ways:

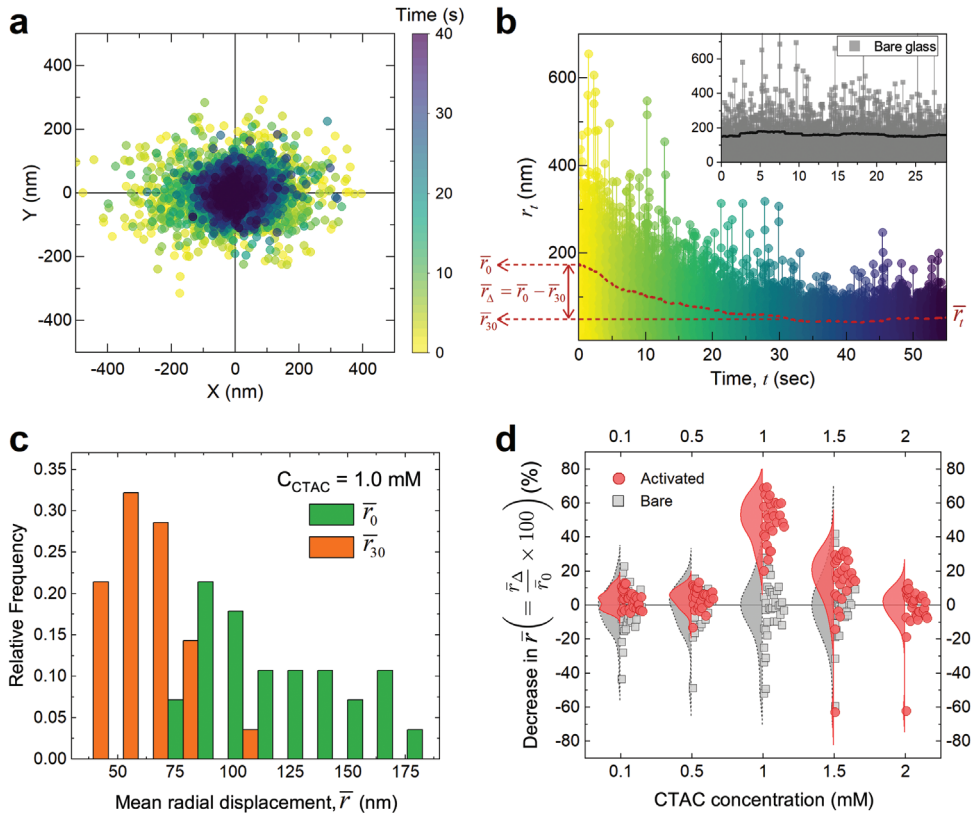

Figure 2. Time-varying motion of particles in harmonic optical traps. a) Position distribution of a single optically-trapped particle near an activated glass wall, color-mapped with time. The *XY* coordinates are defined on a plane parallel to the glass surface, and the origin is aligned with the laser trap center along the laser propagation direction. b) Radial displacements (defined in Equation (2)) as a function of time for the same particle in (a). The red-dashed line indicates a moving average ($\overline{r}_t$) with a subset size of 1730 data points. The inset shows the radial displacement of the same kind of particle at the water/bare glass interface for comparison; the grey solid line shows the same moving average. c) Histograms of the mean radial displacements at $t = 0$ and 30 s. The particles were trapped at $t = 0$ s and stayed in the optical trap for 30 s or more. From (a) to (c), the CTAC concentration was 1.0 mM, and the glass surface was activated by O_2-plasma treatment. d) Comparison of the decreases in $\overline{r}$ for the first 30 s between the bare and activated surfaces as a function of CTAC concentration. The reduced amount, $\overline{r}_\Delta$, is expressed as a percentage of its initial value, $\overline{r}_0$.

1) comparing the behavior of $\overline{r}_t$ between bare and activated glass surfaces and 2) varying the CTAC concentration which provides different adsorption states, for example, surface coverage and aggregate structures. To facilitate the comparisons between the different surfaces and among different concentrations, we quantified the amount of long-term decrease by the difference in the value of $\overline{r}_t$ during the first 30 s of trapping:

$$\overline{r}_\Delta = \overline{r}_0 - \overline{r}_{30} \tag{3}$$

which is also indicated as a red arrow in Figure 2b. We chose the time window of 30 s as it is a typical length of each recording, and (not all but) most of the particles reach a steady state within this period.

We performed dozens of measurements for each of the experimental conditions to average out the effect of experimental variations such as variances in particle sizes and/or charges, and the inhomogeneity of glass surfaces. Different trajectories in Figure S3, Supporting Information demonstrate these variances within the same experimental conditions. Figure 2c illustrates an example analysis for 28 measurements at 1.0 mM CTAC with activated surfaces. The $\overline{r}_0$ represents the average displacement immediately after trapping, whereas the $\overline{r}_{30}$ represents the average displacement after staying 30 s in the optical trap. In that case, the overall left-shift of the histogram toward smaller values indicates the converging trends of particle footprints for randomly chosen particles in random locations.

We tested five different concentrations (0.1, 0.5, 1.0, 1.5, and 2.0 mM), which cover the range below and above the CMC so that each concentration corresponds to different adsorption phases. In general, the extent of surface coverage reaches its maximum near the CMC.[43,46] We found that the CMC of our particle-CTAC mixture is 1.4 mM (Figure S4a, Supporting Information), which is slightly higher than the values reported in the literature (1.0–1.1 mM) due to the existence of the gold colloids in the solution. We refer to our recent publication for more details of the CMC.[56]

Figure 2d summarizes the analyses of the amount of the decrease in $\overline{r}$ for bare and activated substrates as a function of CTAC concentration. The reduction in the mean radial displacement, $\overline{r}_\Delta$, is expressed as a percentage of its initial value, $\overline{r}_0$. For each concentration, the data points (32 ± 6 measurements on average) are shown on the right, and the distribution fit is shown on the left. For all the examined concentrations,

the average temporal change is absent for the bare glass cases (as seen in the inset of Figure 2b), with a distribution centered around the origin. It implies that regardless of the surface coverage increase with the concentration, the spherical admicelles on bare glass substrates have no influence on the long-term changes in particle motion.

On the other hand, the average decay in $\bar{r}$ is much noticeable for the activated glasses but only at specific concentrations, notably at 1 and 1.5 mM in Figure 2d. These concentration-dependent results bolster the proposed hypothesis that the particle–surface interaction is responsive to the surfactant morphologies. We will elaborate on the effect of surface coverage and adsorbed morphologies in detail in Section 2.4.

2.3. Surfactant Bilayers on Particle Surfaces

The stark contrast of the particle motion between the bare and activated surfaces proves that the arrangement of the surfactant molecules at the water–glass interface determines whether or not long-term particle–surface interactions occur. One remaining question is why these interactions occur only with the bilayer structures and not with the globular aggregates.

To answer this question, we also need to consider the surface of the particles. The particle surface before mixing with the surfactant solution is initially covered with citrate anions, used as stabilizing agent. On the addition of surfactant solution, the CTA^+ cations adsorb on the citrate-capped gold surfaces due to electrostatic attraction. According to a recent study by Li et al.,[45] the self-assembly structure of CTA^+ cations on citrate-capped gold surfaces undergoes, with increasing concentration, a gradual transition in the following order: incomplete monolayer → complete monolayer → imperfect bilayer → perfect bilayer → (perfect bilayer + micelles). In our previous study,[56] we found a good agreement between this model proposed by Li et al.[45] and our experimental measurements of colloidal properties. We invite the readers to our publication[56] for detailed discussions and here we give a summarized description in the following.

At the lowest concentration in our system, the surfactants seem to form imperfect bilayer on the particle surfaces. If the surfactant self-assembly formed monolayers (a prior stage before bilayer formation), the particles readily aggregates due to the hydrophobic interactions among the hydrocarbon tails exposed to the bulk fluid.[45] Since we did not find any indication of aggregation in our size measurement using dynamic light scattering (Figure S4c, Supporting Information), we postulated that the surfactant molecules form (imperfect) bilayer structures at the lowest concentration.

The first layer of this bilayer consists of surfactant molecules adsorbed to the gold surface by electrostatic attraction. The second layer comprises molecules adsorbed to the first layer by hydrophobic interactions (similar to the bilayer formation on a flat surface). For this bilayer formation, the completion of the first layer precedes the initiation of the second layer.[45] The fractional coverage of the second layer then gradually increases with concentration. We experimentally confirmed the gradual growth of the second layer by concomitant increases in the particles' zeta potential (Figure S4b, Supporting Information).

Once the bilayer formation is complete on the particles' surfaces and the surfactant concentration is higher than the CMC, micelles in the bulk fluid can also be associated with the particle surface.[45] By measuring the hydrodynamic size of the particles, we discovered the involvement of adsorbed micelles near the particles. In Figure S4c, Supporting Information, the abrupt decrease in the hydrodynamic size above the CMC indicates a decrease in the thickness of the electric double layer due to the increase in local ionic concentration. This can be interpreted as the presence of micelles strongly associated with the particle surface. The particle drawings in **Figures 3** schematically illustrates the developments of adsorbed surfactant morphologies on the particles' surfaces.

To summarize, the surfactant bilayers are present at both the water–glass interface and the particle surface in case of the activated glass. Their structural resemblance can be the key to understanding their interactions. For instance, these bilayers can be more likely to merge, similar to the fusion of lipid bilayers in life.[57,58] In general, bilayers are known as a highly mobile structure.[59] As a result, the outer layer can migrate over the first layer without leaving the surface completely.[46] The first layer, which is electrostatically adsorbed on the surface, can be more tightly bound and not easily dissociated with the surface. Therefore, when the two bilayers come close in the instances of particle trapping, a disruption and rearrangement of the outer layers may occur, resulting in changes in particle behaviors.

2.4. Effects of Bilayer Coverages on Long-Term Interactions

Figures 3a and 3c illustrate the likely development of the surfactant morphologies over the investigated concentration range. We studied in depth the particle behaviors on bare glass substrates (Figure 3a) in our previous work.[56] Here we focus more on the difference between bare and activated surfaces, and especially, on the particles' behaviors on bilayer membranes (Figure 3c) and their long-term interactions (Figure 3b).

Before going into detailed discussions, we make two assumptions about this system. First, we assume that the particle–glass distance remains similar regardless of surfactant concentration. We found experimental evidence that the drag coefficient, which is sensitive to the particle–glass distance,[60] remains similar over the whole concentration range in our previous analysis of the same system with bare glass.[56] This result is counter-intuitive as we expect that the particle's vertical position is determined by the balance between the radiation pressure of the laser beam and the electrostatic repulsion between the two charged surfaces, and the surface charge (and thus the repulsion potential) increases with concentration. A possible scenario is that the surfactant molecules adsorbed at the contact area migrate outside of this region due to the electrostatic repulsion. This explains why the particle height is not determined by the overall concentration. In addition, this assumption still holds for the activated glass as bilayers are also known to be highly mobile. The second assumption is that the effect of surfactants in the bulk solution is insignificant in long-term reactions. As supporting evidence, long-term changes were not observed in the bare glass case across the whole concentration range tested in this study (Figure 2d). This implies that

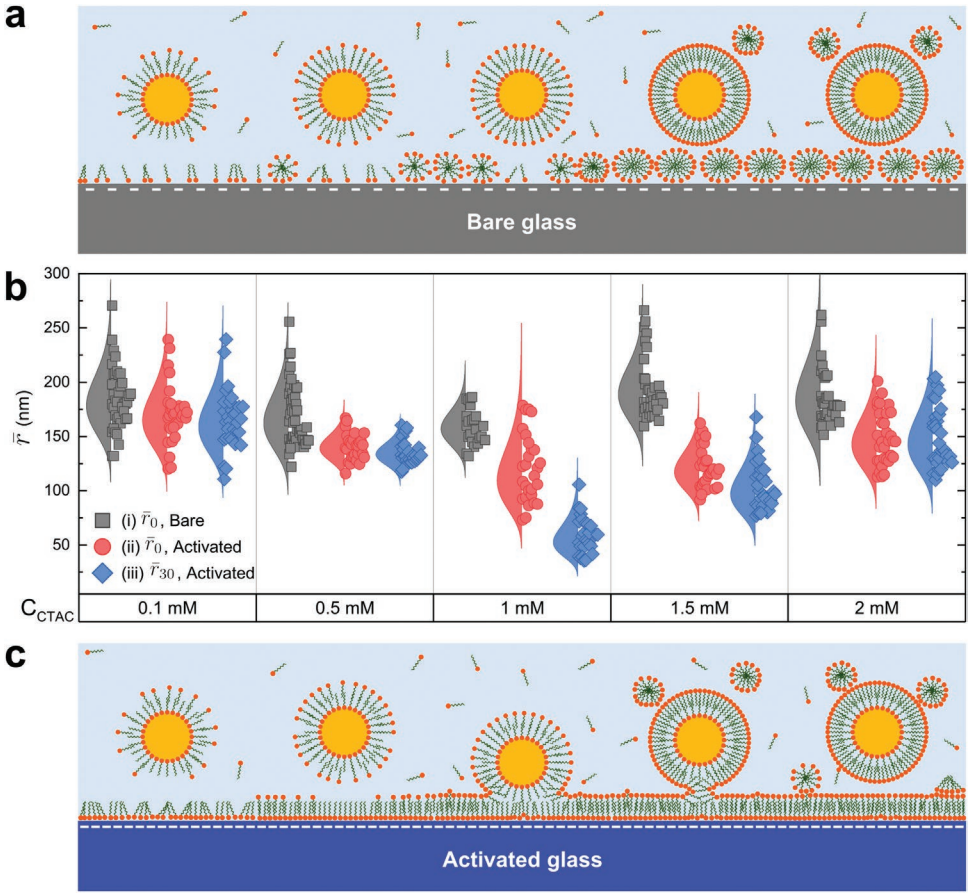

Figure 3. Effects of surfactant morphologies on particle motion as a function of concentration. a) and c) Cartoons showing plausible surfactant self-assembly formations at the gold/water and glass/water interfaces. When the glass surface is activated with O_2-plasma treatment, the adsorbed surfactant structure is assumed to undergo a structural change from globular aggregates to bilayers. The changes in surface coverage and aggregate morphologies is depicted according to the surfactant concentration. b) Distributions of mean radial displacement ($\bar{r}$) as a function of CTAC concentration. Three datasets are displayed side by side for comparison: i) $\bar{r}_0$, bare glass, ii) $\bar{r}_0$, activated glass, and iii) $\bar{r}_{30}$, activated glass.

the surfactants in the bulk solution are of little effect in long-term behaviors, whether they exist as monomers below the CMC (0.1, 0.5, and 1.0 mM) or micelles above the CMC (1.5 and 2.0 mM).

Figure 3b shows the summary of trajectory analyses, quantified as the statistics of the mean radial displacement, $\bar{r}_t$, as a function of CTAC concentration. Each data point was calculated from an independent measurement of single-particle trajectory. Three datasets are plotted side by side for comparison: (i) the initial mean ($\bar{r}_0$) for bare glass, (ii) the initial mean ($\bar{r}_0$) for activated glass, and (iii) the mean after 30 s ($\bar{r}_{30}$) for activated glass. The distribution of $\bar{r}_{30}$ for bare glass is not shown in Figure 3b for clarity as it remains similar to $\bar{r}_0$ in (i). The data points in (ii) and (iii) were calculated from the same dataset as they refers to the initial and steady-state values, respectively.

A comparison among (i), (ii), and (iii) across different concentrations provides qualitative insights into the mechanisms that govern the particles motions on different surfaces: one is the hydrophobic interaction between the particle and the surface, and the other is the extent of bilayer coverage. Compared to admicelles, the primary distinction of bilayer structure is that the hydrophobic interiors can be exposed to the bulk fluid. The exposed hydrophobic groups on a glass surface can interact with hydrophobic groups on a particle surface when the particle approaches. The resulting attraction force explains the decrease in $\bar{r}$ for the bilayer structures in Figure 3b compared to the spherical ones. An exception occurs, however, at the lowest concentration (0.1 mM), where the structural difference at this low coverage is negligible.

On the other hand, the coverage extent determines how much and how fast the $\bar{r}$ decrease will be. When a particle is brought to the surface by the optical tweezer, the hydrophobic interaction brings the particle closer to the surface. As a result, the charged head groups can be disrupted and rearranged, creating a hydrophobic patch below the particle (as illustrated below the second particle in Figure 3c) and, consequently, developing an electrostatic trapping potential. The size of the hydrophobic patch in the bilayer membrane will determine how tight the confinement will be. At low coverages, the confinement of the particle will be moderate, and the reaction will take place promptly as there are a relatively small number of molecules to rearrange. The results at the second lowest concentration (0.5 mM) in Figure 3b support this idea. They show a relatively modest decrease in $\bar{r}$ compared to higher concentrations

(1 or 1.5 mM); furthermore, this decrease happens in the early stage of the trapping so that we do not see much differences between $\overline{r}_0$ and $\overline{r}_{30}$. The variance of the distribution of $\overline{r}$ also decreases significantly, compared to that at the lowest concentration. In other words, the rearrangement process seems to reduce the effect of experimental variations originating from surface heterogeneity.

As the coverage increases with concentration, the overall hydrophobic area (i.e., the exposed hydrophobic regions of the first layer) shrinks, and the surfactant bilayer surrounds a trapped particle more tightly, as depicted in Figure 3c. The dramatic decrease in $\overline{r}$ at 1.0 mM supports this explanation. Other noticeable differences at this concentration are the long-term decrease in $\overline{r}$ over tens of seconds (from $\overline{r}_0$ in (ii) to $\overline{r}_{30}$ in (iii)) and the broadened distribution of $\overline{r}_0$ in (ii). These two phenomena can be closely related and understood by the following explanation. The slow interaction can be a consequence of a two-step process. The incomplete particle bilayer is first combined with the nearest hydrophobic patches on the glass surface (the initial response related to $\overline{r}_0$). This contact domain then gradually grows by taking in other hydrophobic patches that were initially not in the immediate vicinity but slowly diffused over the surface to the particle location (the transition from $\overline{r}_0$ to $\overline{r}_{30}$).[34] Due to the random nature of the surface states, this process can happen at various rates (as shown in Figure S3, Supporting Information), which can result in the broad distribution of $\overline{r}_0$ in the initial stage of the process. Such a slow diffusion is less obvious at 1.5 mM in Figure 3b. This can be interpreted as that the bilayer coverage has almost reached its saturation at this concentration near the CMC (as expected in general[46]), and there are hardly any exposed hydrophobic interiors nearby that can diffuse and cooperate.

As a side note, a similar effect of rearrangements can also occur with spherical admicelles,[56] shown as a slight decrease in $\overline{r}_0$ in (i) when increasing the CTAC concentration from the lowest concentration up to the full coverage concentration in Figure 3b. However, the effect seems much more limited than in the bilayer case due to the low mobility of spherical admicellar structures.

At the highest concentration (2.0 mM) above the CMC, the effect of bilayer interaction is further reduced. The particles' zeta potentials have increased due to micelles' association with the particle surface (Figure S4, Supporting Information). This can be interpreted as the completion of the particle bilayer. We also expect a full surface coverage on the glass surface at this concentration higher than the CMC. As a result, the complete bilayers and stronger electrostatic repulsion between the particle and the surface can hamper the interaction (the last particle in Figure 3c). Accordingly, the $\overline{r}$ recovers its mean and variance comparable to those at the lowest concentration.

With the optical tweezer, which provides a facile manipulation of the particle location with the assistance of precise piezoelectric control, we also observed a "memory effect" while we disturbed the stable trapping by relocating the particle to a new place and bringing it back a few seconds later. Video S1, Supporting Information shows such a particle recording at 1 mM CTAC, where the long-term particle–surface interaction is most apparent. At the beginning of the recording, it shows a particle stably trapped after reaching its steady state (i.e., an equilibrium) at the center. At around 3 s of the timestamp in the video, the particle is moved to a new location on the left side where it becomes immediately destabilized and settles down slowly, similar to our previous observations at this CTAC concentration. The particle stays in this new trap position for about 8 s and is moved back to the original location. Surprisingly, at the original trap location, the particle instantly recovers its stabilized motion. Such an immediate recovery attests to the depletion of the surfactant bilayer at the optical trap, which remains even after the particle leaves the place. It also implies that the back diffusion of molecules to this depleted area is reciprocally a slow process.

2.5. Statistical Analyses of a Time-Varying Single-Particle Trajectory

We have interpreted particle dynamics by examining particle trajectories and investigating the effect of surfactant morphologies and coverages in particle–surface interactions. So far, we have focused on the statistical mean and variance of $\overline{r}$, changing with time and concentration. On the other hand, each trajectory can also be analyzed further by taking the statistics along its time axis. The time-averaged mean squared displacement (MSD) is the most common measure when we deal with particle trajectories. Using the time-averaged MSD, for example, we can analyze the forces acting on the particle, based on a priori knowledge of particle dynamics.[1,61] To be more precise, we first formulate a Langevin equation to describe the motion of a particle and compare the measured MSD with the MSD solved for the Langevin equation. Any deviation from the theoretically solved MSD can prove the involvement of additional forces or interactions.

A particle in an optical trap can be modeled as a damped harmonic oscillator in a fluid with a Langevin equation:[61]

$$m\ddot{x}(t)+\gamma\dot{x}(t)+\kappa x(t)=F_{therm}(t) \tag{4}$$

where m is its inertial mass, γ is its damping (fluid friction) coefficient, κ is the spring constant of the optical trap, and F_{therm} is the random thermal force. The inertial term, $m\ddot{x}(t)$, can be omitted from the equation for describing a particle in an aqueous medium on a timescale longer than a few microseconds.[62] The solution for MSD to the Langevin equation without the inertial term becomes:[61]

$$\mathrm{MSD}_{\mathrm{Langevin}}(\tau)=\frac{2k_BT}{\kappa}\left(1-e^{-\tau\kappa/\gamma}\right) \tag{5}$$

where k_B is the Boltzmann constant and T the temperature.

To attest to the involvement of additional forces arising from the particle–surface interactions, we calculated the time-averaged MSD from the measured trajectory shown in Figure 2a. This trajectory, $\mathbf{T}_N$, is a time-series position data of length N:

$$\mathbf{T}_N=\{(X_1,Y_1),(X_2,Y_2),\ldots,(X_N,Y_N)\} \tag{6}$$

where each position is defined in a 2D space. For this trajectory, $\mathbf{T}_N$, the time-averaged MSD is defined as follows:[1]

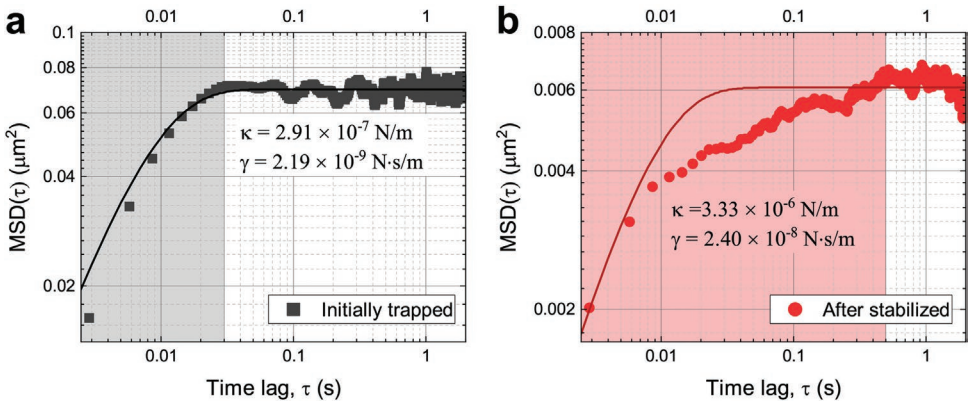

Figure 4. Time-averaged mean squared displacement (MSD) of segmented trajectories. a) Time-averaged MSD calculated from the first five-second segment of the trajectory shown in Figure 2a. The MSD solution of the Langevin equation in 2D (black solid line) is fitted to the measured MSD (grey squares). b) Time-averaged MSD from a segment of the same trajectory after reaching a steady state (red circles). The 2D solution of the Langevin equation (red solid line) is fitted to the data, with constraints on κ and γ to keep the fitted curve within the upper and lower limits of the measured MSD. The shaded areas in (a) and (b) indicate the time lags to reach the MSD plateaus.

$$\mathrm{MSD}_{\mathrm{measured}}(\tau)=\frac{1}{N-\tau}\sum_{i=1}^{N-\tau}\{(X_{i+\tau}-X_i)^2+(Y_{i+\tau}-Y_i)^2\} \quad (7)$$

for any time lag $\tau = 1, 2, \ldots, N-1$. We subdivided the trajectory into five second-long segments and calculated the time-averaged MSD for the first segment ($t = 0 - 5$ s) and another segment after reaching the steady state ($t = 50 - 55$ s) for comparison.

The first segment corresponds to the timespan when the particle has just been trapped and initiated any interaction. The MSD calculated from this segment using Equation (7) is plotted in **Figure 4**a in a double logarithmic scale. The next step is to fit the $\mathrm{MSD}_{\mathrm{Langevin}}$ to this MSD obtained from the experiment. However, the solution given in Equation (5) is for a one-dimensional trajectory. Since we used the measured trajectory defined in two dimensions (Equation (7)), the solution of the Langevin equation should also be multiplied by the trajectory dimension. Therefore, we used a modified solution of the Langevin equation for two dimensions ($=2\times MSD_{\mathrm{Langevin}}(\tau)$) to fit it to the measured MSD. Before executing the curve fitting, we also estimated the temperature K at the particle to be 366.61 K, a value calculated from an electromagnetic heating simulation (Section S5, Supporting Information for more details). Then we estimated the values of the spring (κ) and damping (γ) constants in the least-squares sense as shown in Figure 4a. The measured MSD shows a good agreement with the theoretical MSD, implying that the Langevin equation successfully describes the initially trapped particle motions.

Since we know the average size of the particle, we can also roughly estimate the drag coefficient γ using Stokes' drag (the frictional force exerted on a spherical object in a viscous fluid): $\gamma_{Stokes} = 3\pi\eta d$, where η is the viscosity of the fluid and d the particle diameter. This drag should be corrected further as the particle moves near the glass wall.[63] Assuming that the particle–surface gap is roughly 1/10 of the particle radius, the hydrodynamic drag increases by ≈2.36 times near the surface compared to the Stokes' drag.[64] The drag coefficient, therefore, is approximated as 1.41×10^{-9} N s m^{-1} by assuming the particle diameter $d = 150$ nm and the viscosity $\eta = 0.423$ mPa s for water viscosity at 340 K (Section S5 and Figure S5, Supporting Information for the water temperature simulation). This value of γ is comparable to the value we found from the curve fitting of $\mathrm{MSD}_{\mathrm{Langevin}}$ to the measured MSD (2.19×10^{-9} N s m^{-1}). The discrepancy between them can be attributed to any mismatch between the assumptions and the actual values for the particle size and water viscosity. It can also be attributed to the particle–surface interaction during the first five trapping seconds.

In contrast to the initial segment, the MSD calculated from the segment after reaching the steady state exhibits an anomalous behavior that is significantly deviating from the theoretical prediction (Figure 4b). For the curve fitting in this case, we applied a boundary condition for κ and γ ($0 < \kappa < 4 \times 10^{-6}$; $0 < \gamma < 2.4 \times 10^{-8}$) to keep the fitted curve between the minimum and maximum values of the measured MSD for the measured time lags. The estimated value for κ has increased about ten times compared to the value fitted to the initial segment. It supports our hypothesis that the rearrangement of the incomplete bilayer can create a complementary trapping potential. The estimated drag, γ, has also increased about ten times, likely due to the increased restrictions in particle motion imposed by the bilayer interactions based on our hypothesis. Most importantly, the Langevin equation now fails to describe the motion of the particle after reaching the steady state. This implies that the particle does not behave like a damped harmonic oscillator anymore, suggesting the emergence of a new type of force or physical interaction such as the fusion of the bilayers, as we suggested earlier.

Some theoretical works also suggest that the subdiffusive behavior between $\tau = 0.01$ s and 0.5 s in Figure 4b can represent geometrical confinement.[65,66] Furthermore, several experiments in biology reported similar findings that the subdiffusive motions of probe molecules were caused by increased obstruction such as polymer networks in the cytoplasm[67] or the presence of the cell nuclei.[68] In addition, a very similar time-averaged MSD dependence on τ was also reported by Jeon et al.[69] with a polystyrene bead in a worm-like micellar solution, where the elongated micelles form a transient polymer network. They explained that such a characteristic subdiffusive motion in the millisecond range resembles the movement

of a particle in a viscoelastic medium. These theoretical and experimental findings provide solid evidence that the particle in Figure 4b experiences geometrical confinement and a coincident viscoelastic effect, which can be related to the interactions among surfactant molecules. However, an important difference in our case is that these interactions were constrained to the interface since the surfactant concentration was below the CMC, that is, prior to the micelle formation in the bulk solution. Therefore, the MSDs in Figure 4a,b corroborate the idea of the bilayer rearrangement and the partial fusion proposed in the previous section.

3. Conclusions

We have examined the trajectories of colloidal particles locally confined at a water–glass interface by an optical tweezer. These optically bright particles act as a nanoscale probe that can respond to various changes in surfactant self-assemblies adsorbed at the solid–liquid interfaces. Such changes include the development of surfactant coverages during the adsorption process, morphological changes induced by surface preparation, and dynamic interactions between particles and surfaces. The statistics of single-particle trajectories provided information on the average particle behaviors, which were also well correlated with the adsorption phase described in the literature.[46] Individual trajectories, on the other hand, showed local and dynamic behaviors of the adsorbed molecules in real time, which have been obscured in traditional thermodynamic experiments. We analyzed the spatial and temporal motions of optically trapped particles and provided new insights into the interactions governing the particle motions at the nanoscale. Especially, by studying the unique system consisting of a gold nanoparticle, a glass–water interface, and surfactants, we found evidence of the fusion of surfactant bilayers at the narrow gap between the particle and the surface. Our findings demonstrate the great potential of optically trapped nanoparticles as a probe to investigate real-time chemical processes at the nanoscale. In particular, we expect that this marriage of SPT and optical manipulation can also shed new light on even more complex interfacial phenomena when combined with recent developments in three-dimensional SPT[37] and high-speed imaging.[70]

4. Experimental Section

Materials: Gold colloids with 150 nm diameter, stabilized in citrate buffer, were purchased from Sigma-Aldrich (a product of CytoDiagnostics, Inc.). CTAC was obtained from Sigma-Aldrich (25 wt% in H_2O) and diluted the solution with distilled water to reach desired concentrations ranging from 0.1 to 2.0 mM. A separate gold nanoparticle-CTAC mixture is prepared for each CTAC concentration. The stock gold colloids were centrifuged for 30 min at 200 × *g* for separation and re-dispersed using a vortex mixer in a CTAC solution at a desired concentration. The concentration of gold nanoparticles was further reduced in order to have a sparse appearance under an optical microscope and thus ensure single-particle trapping. The dispersity of gold nanoparticles in surfactant solution was confirmed by zeta potential and hydrodynamic size measurements (Figure S4, Supporting Information) using dynamic light scattering (Zetasizer Nano ZS, Malvern Panalytical). A pair of borosilicate glass coverslips (145 µm in thickness) and a double-sided adhesive spacer (120 µm thickness, Grace Bio-Labs SecureSeal imaging spacer) were used to build a fluid chamber. All the trapping experiments were performed inside the fluid chamber to keep the liquids from evaporating.

Preparation of Glass Surface: Starting with borosilicate glass coverslips (Menzel Gläser), two different types of glass surfaces were prepared to alter the adsorbed morphologies of the surfactant molecules. One type of glass is native glass without any surface modification. The other type of glass is treated with oxygen plasma (at 200 W for 60 s with a 400 mL min^{-1} flowrate) to activate its surface.[53] The plasma-treated glasses were immediately used to prepare the fluid chambers so that the time between the surface treatment and the sample preparation is minimized. All glass coverslips were sonicated in acetone and isopropyl alcohol baths for 30 minutes each, before use or surface modification.

Optical Trapping and Video Analysis of a Trapped Particle: In each experiment, a single gold nanoparticle was optically trapped near a glass wall using a He-Ne laser. A dry objective lens (60×, 0.85 NA) was used to focus the trapping laser at the water–glass interface. The laser power was controlled to be 10 mW before entering the trapping objective using a laser-line variable beamsplitter (VA5-633, Thorlabs). The trapping objective lens and the sample were mounted on piezoelectric stages to adjust the trap position and the sample location with a nanometer resolution.

Contrary to a typical optical trapping setup, the laser beam was not expanded and therefore did not entirely fill the entrance pupil of the trapping objective lens. The resulting loosely-focused laser beam produced a strong radiation pressure and a weak lateral trap at the chosen power level. As a result, the strong radiation pressure brought the particle close to the glass surface, which played a crucial role in observing the particle–glass surface interactions; simultaneously, the moderate optical restoring force restricted the diffusion of the particle in a confined area. The particle's vertical position was determined by the balance between the radiation pressure of the laser beam and the electrostatic repulsion at the narrow gap between the particle and glass surfaces. For each measurement, the particle was pushed toward the glass surface until it was most stably trapped laterally. This implied that the beam waist was located where the radiation pressure and the electrostatic repulsion canceled each other.

Figure S6, Supporting Information shows the schematic of the optical trapping and imaging system used in this study. The imaging setup operates in high-angle annular dark-field (HAADF) mode, which eliminates the signals from the background. As a result, the gold nanoparticles appear as a bright optical probe, enabling high-speed image acquisition compared to that of the low-intensity fluorescence counterparts.[15] The particle motion within an optical trap was recorded using a CMOS camera (CM3-U3-50S5C-CS, FLIR) at a 346 framerate. Each measurement recorded a sub-region of the CMOS sensor in size of 96 × 96 pixels for ≈10 000 frames or more. Two-dimensional particle trajectories (parallel to the glass surface) were traced from time-lapse image data. The authors only analyzed observations with single nanoparticles and excluded those with multiple particles such as an example shown in Video S2, Supporting Information. For tracing, a python toolkit, Trackpy,[71] was used, which is based on a particle-tracking algorithm developed by Crocker et al.[72] The temporal and spatial resolutions of a trajectory were, respectively, determined by the camera frame rate (1/346 ≈ 3 ms) and the camera pixel size divided by the image magnification (3450/60 = 57.5 nm per pixel).

Supporting Information

Supporting Information is available from the Wiley Online Library or from the author.

Supporting Information is available from the authors. A dataset for all the particle recordings and the corresponding trajectories is available in our Zenodo data repository.[73]

Acknowledgements

Funding from the European Research Council (ERC-2015-AdG-695206 Nanofactory) is gratefully acknowledged.

Conflict of Interest

The authors declare no conflict of interest.

Data Availability Statement

The data that support the findings of this study are openly available in Zenodo at https://doi.org/10.5281/zenodo.6015007, reference number 5941496.

Keywords

adsorption, bilayer membrane, gold nanoparticle, optical tweezers, self-assembly, single-particle tracking, surfactant

Received: August 19, 2022
Revised: November 23, 2022
Published online: December 16, 2022

[1] H. Qian, M. Sheetz, E. Elson, *Biophys. J.* **1991**, *60*, 910.
[2] M. J. Saxton, K. Jacobson, *Annu. Rev. Biophys. Biomol. Struct.* **1997**, *26*, 373.
[3] T. Fujiwara, K. Ritchie, H. Murakoshi, K. Jacobson, A. Kusumi, *J. Cell Biol.* **2002**, *157*, 1071.
[4] M. C. Beckerle, *J. Cell Biol.* **1984**, *98*, 2126.
[5] T. Franosch, M. Grimm, M. Belushkin, F. M. Mor, G. Foffi, L. Forró, S. Jeney, *Nature* **2011**, *478*, 85.
[6] H. Geerts, M. De Brabander, R. Nuydens, S. Geuens, M. Moeremans, J. De Mey, P. Hollenbeck, *Biophys. J.* **1987**, *52*, 775.
[7] H.-M. Wu, Y.-H. Lin, T.-C. Yen, C.-L. Hsieh, *Sci. Rep.* **2016**, *6*, 20542.
[8] A. Gahlmann, W. E. Moerner, *Nat. Rev. Microbiol.* **2014**, *12*, 9.
[9] A. Kusumi, T. A. Tsunoyama, K. M. Hirosawa, R. S. Kasai, T. K. Fujiwara, *Nat. Chem. Biol.* **2014**, *10*, 524.
[10] Y.-P. Chang, F. Pinaud, J. Antelman, S. Weiss, *J. Biophotonics* **2008**, *1*, 287.
[11] N. Ruthardt, D. C. Lamb, C. Bräuchle, *Mol. Ther.* **2011**, *19*, 1199.
[12] C. Manzo, M. F. Garcia-Parajo, *Rep. Prog. Phys.* **2015**, *78*, 124601.
[13] S. Spindler, J. Ehrig, K. König, T. Nowak, M. Piliarik, H. E. Stein, R. W. Taylor, E. Garanger, S. Lecommandoux, I. D. Alves, V. Sandoghdar, *J. Phys. D* **2016**, *49*, 274002.
[14] R. W. Taylor, R. G. Mahmoodabadi, V. Rauschenberger, A. Giessl, A. Schambony, V. Sandoghdar, *Nat. Photon.* **2019**, *13*, 480.
[15] H. Shen, L. J. Tauzin, R. Baiyasi, W. Wang, N. Moringo, B. Shuang, C. F. Landes, *Chem. Rev.* **2017**, *117*, 7331.
[16] J. C. Araque, S. K. Yadav, M. Shadeck, M. Maroncelli, C. J. Margulis, *J. Phys. Chem. B* **2015**, *119*, 7015.
[17] J. Kirstein, B. Platschek, C. Jung, R. Brown, T. Bein, C. Bräuchle, *Nat. Mater.* **2007**, *6*, 303.
[18] D. A. Higgins, S. C. Park, K.-H. Tran-Ba, T. Ito, *Annu. Rev. Anal. Chem.* **2015**, *8*, 193.
[19] D. G. Grier, *Curr. Opin. Colloid Interface Sci.* **1997**, *2*, 264.
[20] K. C. Neuman, S. M. Block, *Rev. Sci. Instrum.* **2004**, *75*, 2787.
[21] O. M. Maragó, P. H. Jones, P. G. Gucciardi, G. Volpe, A. C. Ferrari, *Nat. Nanotechnol.* **2013**, *8*, 807.
[22] R. W. Bowman, M. J. Padgett, *Rep. Prog. Phys.* **2013**, *76*, 026401.
[23] G. V. Philip, H. Jones Onofrio, M. Maragó, in *Optical Tweezers: Principles and Applications*, Cambridge University Press, Cambridge **2015**.
[24] C. J. Bustamante, Y. R. Chemla, S. Liu, M. D. Wang, *Nat. Rev. Methods Primers* **2021**, *1*, 25.
[25] A. Ashkin, J. M. Dziedzic, J. E. Bjorkholm, S. Chu, *Opt. Lett.* **1986**, *11*, 288.
[26] A. Ashkin, J. M. Dziedzic, *Science* **1987**, *235*, 1517.
[27] A. Ashkin, J. M. Dziedzic, T. Yamane, *Nature* **1987**, *330*, 769.
[28] K. Svoboda, C. F. Schmidt, B. J. Schnapp, S. M. Block, *Nature* **1993**, *365*, 721.
[29] M. Wang, H. Yin, R. Landick, J. Gelles, S. Block, *Biophys. J.* **1997**, *72*, 1335.
[30] M. J. Lang, P. M. Fordyce, A. M. Engh, K. C. Neuman, S. M. Block, *Nat. Methods* **2004**, *1*, 133.
[31] M. J. Comstock, T. Ha, Y. R. Chemla, *Nat. Methods* **2011**, *8*, 335.
[32] A. Yao, M. Tassieri, M. Padgett, J. Cooper, *Lab Chip* **2009**, *9*, 2568.
[33] M. Polin, D. G. Grier, S. R. Quake, *Phys. Rev. Lett.* **2006**, *96*, 088101.
[34] R. Walder, N. Nelson, D. K. Schwartz, *Phys. Rev. Lett.* **2011**, *107*, 156102.
[35] M. J. Skaug, J. N. Mabry, D. K. Schwartz, *J. Am. Chem. Soc.* **2014**, *136*, 1327.
[36] B. Dong, Y. Pei, F. Zhao, T. W. Goh, Z. Qi, C. Xiao, K. Chen, W. Huang, N. Fang, *Nat. Catal.* **2018**, *1*, 135.
[37] Y. Zhong, G. Wang, *Annu. Rev. Anal. Chem.* **2020**, *13*, 381.
[38] P. Atkins, J. De Paula, in *Atkins' Physical Chemistry*, Oxford University Press, Oxford, UK **2014**.
[39] Y. Yuan, Y. Lin, B. Gu, N. Panwar, S. C. Tjin, J. Song, J. Qu, K.-T. Yong, *Coord. Chem. Rev.* **2017**, *339*, 138.
[40] N. Oyamada, H. Minamimoto, K. Murakoshi, *J. Am. Chem. Soc.* **2022**, *144*, 2755.
[41] Y. Tsuboi, S. Naka, D. Yamanishi, T. Nagai, K.-i. Yuyama, T. Shoji, B. Ohtani, M. Tamura, T. Iida, T. Kameyama, T. Torimoto, *ACS Appl. Nano Mater.* **2021**, *4*, 11743.
[42] W. A. Ducker, E. J. Wanless, *Langmuir* **1999**, *15*, 160.
[43] E. Tyrode, M. W. Rutland, C. D. Bain, *J. Am. Chem. Soc.* **2008**, *130*, 17434.
[44] E. Evans, D. Needham, *J. Phys. Chem.* **1987**, *91*, 4219.
[45] R. Li, Z. Wang, X. Gu, C. Chen, Y. Zhang, D. Hu, *ACS Omega* **2020**, *5*, 4943.
[46] R. Atkin, V. Craig, E. Wanless, S. Biggs, *Adv. Colloid Interface Sci.* **2003**, *103*, 219.
[47] T. P. Goloub, L. K. Koopal, B. H. Bijsterbosch, M. P. Sidorova, *Langmuir* **1996**, *12*, 3188.
[48] T. P. Goloub, L. K. Koopal, *Langmuir* **1997**, *13*, 673.
[49] R. E. Lamont, W. A. Ducker, *J. Am. Chem. Soc.* **1998**, *120*, 7602.
[50] M. Chorro, C. Chorro, O. Dolladille, S. Partyka, R. Zana, *J. Colloid Interface Sci.* **1999**, *210*, 134.
[51] L. M. Grant, T. Ederth, F. Tiberg, *Langmuir* **2000**, *16*, 2285.
[52] S. H. Behrens, D. G. Grier, *J. Chem. Phys.* **2001**, *115*, 6716.
[53] A. U. Alam, M. M. R. Howlader, M. J. Deen, *J. Micromech. Microeng.* **2014**, *24*, 035010.
[54] J. P. Kottmann, O. J. F. Martin, D. R. Smith, S. Schultz, *Chem. Phys. Lett.* **2001**, *341*, 1.
[55] R. W. Taylor, V. Sandoghdar, *Nano Lett.* **2019**, *19*, 4827.
[56] J. Kim, O. J. F. Martin, *J. Phys. Chem. C* **2022**, *126*, 378.
[57] C. A. Helm, J. N. Israelachvili, P. M. McGuiggan, *Biochem.* **1992**, *31*, 1794.
[58] H. I. Petrache, N. Gouliaev, S. Tristram-Nagle, R. Zhang, R. M. Suter, J. F. Nagle, *Phys. Rev. E* **1998**, *57*, 7014.
[59] P. Atkins, J. De Paula, in *Atkins' Physical Chemistry*, Oxford University Press, Oxford, UK **2014**, Ch. 14, pp. 628–629.
[60] E. Schäffer, S. F. Nørrelykke, J. Howard, *Langmuir* **2007**, *23*, 3654.
[61] S. F. Nørrelykke, H. Flyvbjerg, *Phys. Rev. E* **2011**, *83*, 041103.
[62] E. M. Purcell, *Am. J. Phys.* **1977**, *45*, 3.

[63] J. Happel, H. Brenner, in *Low Reynolds Number Hydrodynamics: With Special Applications to Particulate Media*, Vol. *1*, Springer, Dordrecht **2012**.
[64] K. Svoboda, S. M. Block, *Annu. Rev. Biophys. Biomol. Struct.* **1994**, *23*, 247.
[65] T. Neusius, I. M. Sokolov, J. C. Smith, *Phys. Rev. E* **2009**, *80*, 011109.
[66] J.-H. Jeon, R. Metzler, *Phys. Rev. E* **2010**, *81*, 021103.
[67] I. M. Tolić-Nørrelykke, E.-L. Munteanu, G. Thon, L. Oddershede, K. Berg-Sørensen, *Phys. Rev. Lett.* **2004**, *93*, 078102.
[68] M. Wachsmuth, W. Waldeck, J. Langowski, *J. Mol. Biol.* **2000**, *298*, 677.
[69] J.-H. Jeon, N. Leijnse, L. B. Oddershede, R. Metzler, *New J. Phys.* **2013**, *15*, 045011.
[70] K. Morimoto, A. Ardelean, M.-L. Wu, A. C. Ulku, I. M. Antolovic, C. Bruschini, E. Charbon, *Optica* **2020**, *7*, 346.
[71] D. B. Allan, T. Caswell, N. C. Keim, C. M. van der Wel, R. W. Verweij, soft-matter/trackpy: Trackpy v0.5.0, https://doi.org/10.5281/zenodo.4682814 (accessed: February 2022).
[72] J. C. Crocker, D. G. Grier, *J. Colloid Interface Sci.* **1996**, *179*, 298.
[73] J. Kim, O. J. F. Martin, Dataset for the manuscript: Probing surfactant bilayer interactions by tracking optically trapped single nanoparticles, https://doi.org/10.5281/zenodo.6015007 (accessed: February 2022).